The thermal regime around buried submarine high voltage cables

C. J. Emeana,[1] T. J. Hughes,[1] J. K. Dix,[1] T. M. Gernon,[1] T. J. Henstock,[1] C. E. L. Thompson,[1] and J. A. Pilgrim,[2]

[1]*Ocean and Earth Science, National Oceanography Centre, University of Southampton, Southampton, SO14 3ZH, United Kingdom. E-mail: C.J.Emeana@soton.ac.uk*

[2]*Electronics and Computer Science, University of Southampton, Southampton, SO17 1BJ, United Kingdom.*

SUMMARY

The expansion of offshore renewable energy infrastructure and the need for trans-continental shelf power transmission require the use of submarine High Voltage (HV) cables. These cables have maximum operating surface temperatures of up to 70°C and are typically buried 1-2 m beneath the seabed, within the wide range of substrates found on the continental shelf. However, the heat flow pattern and potential effects on the sedimentary environments around such anomalously high heat sources in the near surface sediments are poorly understood. We present temperature measurements from a 2D laboratory experiment representing a buried submarine HV cable, and identify the thermal regimes generated within typical unconsolidated shelf sediments—coarse silt, fine sand and very coarse sand. We used a large (2 x 2.5 m) tank filled with water-saturated spherical glass beads (ballotini) and instrumented with a buried heat source and 120 thermocouples, to measure the time-dependent 2D temperature distributions. The observed and corresponding Finite Element Method (FEM) simulations of the steady state heat flow regimes, and normalised radial temperature distributions were assessed. Our results show that the heat transfer and thus temperature fields generated from submarine HV cables

buried within a range of sediments are highly variable. Coarse silts are shown to be purely conductive, producing temperature increases of >10 ^{o}C up to 40 cm from the source of 60 °C above ambient; fine sands demonstrate a transition from conductive to convective heat transfer between c. 20°C and 36^{o}C above ambient, with >10^{o}C heat increases occurring over a metre from the source of 55^{o}C above ambient; and very coarse sands exhibit dominantly convective heat transfer even at very low (c. 7^{o}C) operating temperatures and reaching temperatures of up to 18^{o}C above ambient at a metre from the source at surface temperatures of only 18^{o}C. These findings are important for the surrounding near surface environments experiencing such high temperatures and may have significant implications for chemical and physical processes operating at the grain and sub-grain scale; biological activity at both micro-faunal and macro-faunal levels; and indeed the operational performance of the cables themselves, as convective heat transport would increase cable current ratings, something neglected in existing standards.

Keywords: Heat flow; Permeability and porosity; Heat generation and transport.

1. INTRODUCTION

Submarine High Voltage (HV) cables form the backbone of offshore renewable power transmission, and are increasingly important in regional energy distribution over distances of up to 580 km across continental shelves such as the NorNed HV direct current submarine power cable link (Worzyk, 2009). The commercial interest in sub-seafloor HV cables has grown significantly in recent years, particularly as a result of more (larger) wind farms located ever further offshore (EWEA, 2013) and the simultaneous development of trans-national marine cables links such as the Cross Sound HV direct current submarine cable link (Railing *et al.*,

2004) and proposed European Super Grid (UK House of Commons: Energy and Climate Change Committee, 2011). These multi-million pound submarine HV cable links are typically buried by trenching to depths of 1-2 m (Mole *et al.*, 1997, Worzyk, 2009) beneath the seabed and within the wide range of substrates found on the continental shelf, with little knowledge of the thermal regime they will enter or generate during operation.

The present maximum operating conductor temperature of HV cables is 90^{o}C which can translate to cable surface temperatures of up to 70^{o}C (Swaffield *et al.*, 2008, Hughes *et al.*, 2015). This means the surrounding seawater-saturated sediments will experience thermal conditions typically only reached at approximately 2.8 km of burial under normal geothermal gradients (Boehler, 1996, Nagihara and Smith, 2005, Geohil, 2013, Christie and Nagihara, 2016) Despite the potential for such anomalously high temperatures, there has been very limited study on the actual temperatures generated around submarine cables, with only one reported field study (Meissner *et al.*, 2007), and limited numerical modelling work (Worzyk, 2009, Hughes *et al.*, 2015).

There are also only a few papers on the thermal properties of shelf sediments (Lovell, 1985a, Lovell, 1985b, Zimmerman, 1989, Jackson and Richardson, 2001, Kim *et al.*, 2007, Wheatcroft *et al.*, 2007, Goto *et al.*, 2012), and these solely consider conductive heat flow. However, recent numerical modelling by Hughes et al. (2015) suggests that for fully saturated marine sediments, heat transfer can occur by both conduction and convection, depending on cable surface temperature and sediment properties. Hughes et al. (2015) found that permeability is the overarching controlling factor, with the transition from conduction to convection expected as permeability increases to the range 10^{-11}m^2 - 10^{-10}m^2. In continental shelf settings, this means that fine-grained substrates would be predicted to have conductive heat transport, with a transition as grain size increases to convective heat transport in sands. If this is correct, there

are implications for both the environment surrounding the cables, and the current that can be carried by the cables.

As several marine organisms are sensitive to minor ambient temperature changes, any such temperature increases in the surrounding sediment may cause significant impacts and displacements of living organisms dwelling within the near-surface environments (OSPAR, 2009b). The German Federal Maritime and Hydrographic Agency (BSH) have produced environmental regulations which set an acceptable limit of <2K (2^{o}C) above ambient temperature rise at 20 cm below the seabed and directly above the cable (OSPAR, 2009b, BSH, 2014), to minimise impacts on shallow-burrowing organisms. However at the higher operational temperatures, there is also the potential for geochemical changes within the sediments.

In addition to the lack of knowledge of the potential impacts of the heat generated by the cable on the environment, there is also little knowledge of the relationship between the thermal properties of marine sediments and the current that may be reliably carried by submarine HV cables. This is controlled by a balance between resistive heating within the cable and how efficiently heat is lost to the environment, such that the cable remains below its design temperature. In the terrestrial environment the substrate in which they are buried, often involving variability in backfilling during trenching, has a significant effect on cable current ratings (de Leon and Anders, 2008, Swaffield *et al.*, 2008). The IEC 60287 standard (BS-IEC-60287-1-1:2014, 2014) to estimate the current rating of buried cables assumes terrestrial conditions: an isothermal ground temperature, homogeneous burial sediment, conductive heat transfer and a simple model for the thermal resistance of the surrounding sediments. These basic assumptions may not be appropriate in any case for continental shelves given the wide range of substrates and their physical properties (muds, sands, gravels and even bedrock) (van Landeghem *et al.*, 2014), due to natural depositional processes. However, if convective heat

transport occurs, then the greater efficiency may allow significantly higher currents to be carried by the cables.

This paper presents the first set of temperature measurements from a 2D laboratory experiment designed as an analogue to a buried submarine HV cable. We use a range of realistic cable surface temperatures to identify how the thermal regimes and heat transport mechanisms may vary with a range of typical shelf sediments. We compare the results with the predictions of theoretical models, and explore some of the environmental implications.

2. METHOD DEVELOPMENT

2.1. Experimental set-up

Temperature time series data are measured using a 2D experimental tank (height: 2.5 m, width: 2.0 m and thickness: 0.11 m, Figure 1a) filled with prototype scale, tap water saturated, sediments and with an inserted heat source (Figure 1b), designed as a proxy to a buried sub-seafloor HV cable. The heat source is capable of generating cable surface temperatures up to 100^{o}C. This approach is adapted from analogue experiments involving gas-particle fluidization in volcanic systems (Gernon *et al.*, 2008). The tank is constructed from 2 cm thick Perspex, reinforced with steel bars (Figure 1a). The vicat softening temperature, coefficient of thermal expansion and thermal conductivity of the Perspex are 110 ^{o}C, 7x10^{-5} K^{-1}, and 0.2 Wm^{-1} K^{-1}, respectively. The tank is open at the top and has integrated outlets at the base to allow in-fill and removal of sediments and water. Three layers of 10 cm thick Celotex™ TA4000 insulation sheets are directly attached to the external sides of the tank to limit heat loss through the Perspex sides. Each of the attached insulation sheets has a thermal conductivity of 0.022 Wm^{-}

^{1} K^{-1} and low emissivity aluminium foil facings on both sides, providing high performance insulation (Celotex, 2013).

The heat source was constructed using an INC800 heating element (Length: 2.44m and Loading Watt: 2000) that is tightly coiled inside a drilled cavity in the middle of a cylindrical aluminium block (radius: 0.11 m and thickness: 0.10 m), providing a good thermal contact. A variable autotransformer (variac) and voltage stabilizer are used to provide a controlled heat input and stabilise the fluctuating mains output. Water ingress into the cavity of the heat source is prevented using two tightly sealed aluminium side coverings. During the design phase modelling of the heat source (Hughes *et al.*, 2015) ensured an isothermal outer surface could be produced. Subsequently, a number of initial measurements on the heat source were conducted to assess its operation, and to test the predicted isothermal outer surface. Six K6-type thermocouples (hereafter referred to as TCs) were attached equidistantly around the surface of the heat source. The TCs have a solid diameter of 0.376mm and an operating temperature range of -75^{o}C to 250^{o}C, a quoted accuracy of ± 1.5^{o}C and a precision of ± 0.25% (equivalent to ± 0.1-0.3 ^{o}C over the measured temperature range). Each welded 'single shot' tip of the TCs are at the termination point of 5 m long PTFE, water tight, insulated cables. During a pilot study, the heat source was inserted in a small tank filled with a mixture of sediments and water. Measurements from the attached 6 TCs gave surface temperatures at three time steps (0.7, 2.8 and 4.9 days respectively) of 29.7 ±0.1 ^{o}C, 38.6 ±0.1 ^{o}C and 48.2 ±0.2 ^{o}C respectively. The low standard deviation of these measurements (within the quoted precision of the TCs) supports the isothermal heat distribution predicted from the initial modelling.

Temperatures within the tank are measured using 120 of the K6-type TCs attached to nodes on a pre-constructed mesh. The TC grid varied between a nodal spacing of 10 cm and 20 cm with the higher density grid immediately adjacent to the heat source and the central section of the tank (Figure 1c). After installation of the TCs inside the experimental tank, and prior to

adding the sediment, high resolution digital imagery of the TCs along with multiple scales has been taken and the images rectified to locate each TC to an accuracy of 1 mm. Temperature time series measurements are recorded at 60 second intervals on a Campbell Scientific CR1000 measurement control system, with a fixed measurement range of -44 to 80^{o}C for all experiments. The temperature time series data were filtered using a moving average filter with a span of 5 minutes to smooth the remnant variation in the temperature data due to the fluctuating mains output. The TCs are distributed throughout the tank (Figure 1c) to measure the surface temperature of the heat source (1 TC), the temperature distribution within the sediment (113 TCs), the water column at the top of the tank (3 TCs) and the ambient air temperature throughout each experiment (3 TCs externally located at the top and bottom of the tank and on the outermost insulation sheet).

For the experiments presented in this paper, the tank is filled with a mixture of water (undistilled) and ballotini, a synthetic sediment composed of spherical Soda-lime glass beads material made up of 72.0% silicon dioxide (SiO_2), 13.5% sodium oxide (Na_2O), 9.0% calcium oxide (lime, CaO), 3.4% magnesium oxide (MgO), 2.0% aluminium oxide (Al_2O_3) and 0.1% iron oxide (Fe_2O_3) minerals (Potters-Ballotini, 2011). Also the physical characteristics of ballotini are: 2.5 specific gravity, 1172 $JKg^{-1}K^{-1}$ specific heat capacity and 0.94 $Wm^{-1}K^{-1}$ thermal conductivity (Potters-Ballotini, 2011) and measurements from various near surface marine environments with high porosity sediments, demonstrated that thermal conductivity of approximately 1 $Wm^{-1}K^{-1}$ is quite representative for such environments (Woodside and Messmer, 1961, Beck, 1976, Lovell, 1985b, Lovell, 1985a). Thus, ballotini was chosen to ensure uniform composition and size of the grains, and provides greater control of the porosity and permeability as well as enables application of the laboratory experiment results to the natural thermal regimes experienced by submarine HV cables buried within near surface shelf sediments.

Three different pre-sieved, very well sorted, symmetric and mesokurtic samples of ballotini were used. Table 1 shows the measured mean grain sizes ($\boldsymbol{d_m}$) 0.045mm (Coarse Silt), 0.20mm (Fine Sand) and 1.23mm (Very Coarse Sand) of the three size classes and the results are based on sieve analysis, graphical methods of Folk and Ward (Folk and Ward, 1957) in GRADISTAT version 8 (Blott and Pye, 2001) and the Udden-Wentworth grain-size scale for siliciclastic sediments (Wentworth, 1922). The mean and range of porosities ($\boldsymbol{n}$) of the three samples are measured based on the gravimetric grain volume approach (Amyx *et al.*, 1960) and subsequently their permeabilities ($\boldsymbol{k}$) are calculated using the Kozeny-Carman (Carman, 1937) equation (1). The porosity ($\boldsymbol{n}$) estimates are, Coarse Silt: 0.2 ± 0.05; Fine Sand: 0.32 ± 0.06 and Very Coarse Sand: 0.4 ± 0.05. Thus, the corresponding permeability ($\boldsymbol{k}$) estimates and the other measured physical properties of the three different pre-sieved size classes of ballotini are summarised in Table 1 and are consistent with typical estimates of shelf sediments (Bear, 1972, Van Brakel, 1975, Quiblier, 1984, Blair *et al.*, 1996, Turcotte and Schubert, 2002, Jackson and Richardson, 2007, Hughes *et al.*, 2015).

$$\boldsymbol{k = \frac{1}{180}\frac{n^3}{(1-n)^2}d_m^2} \qquad (\mathbf{1})$$

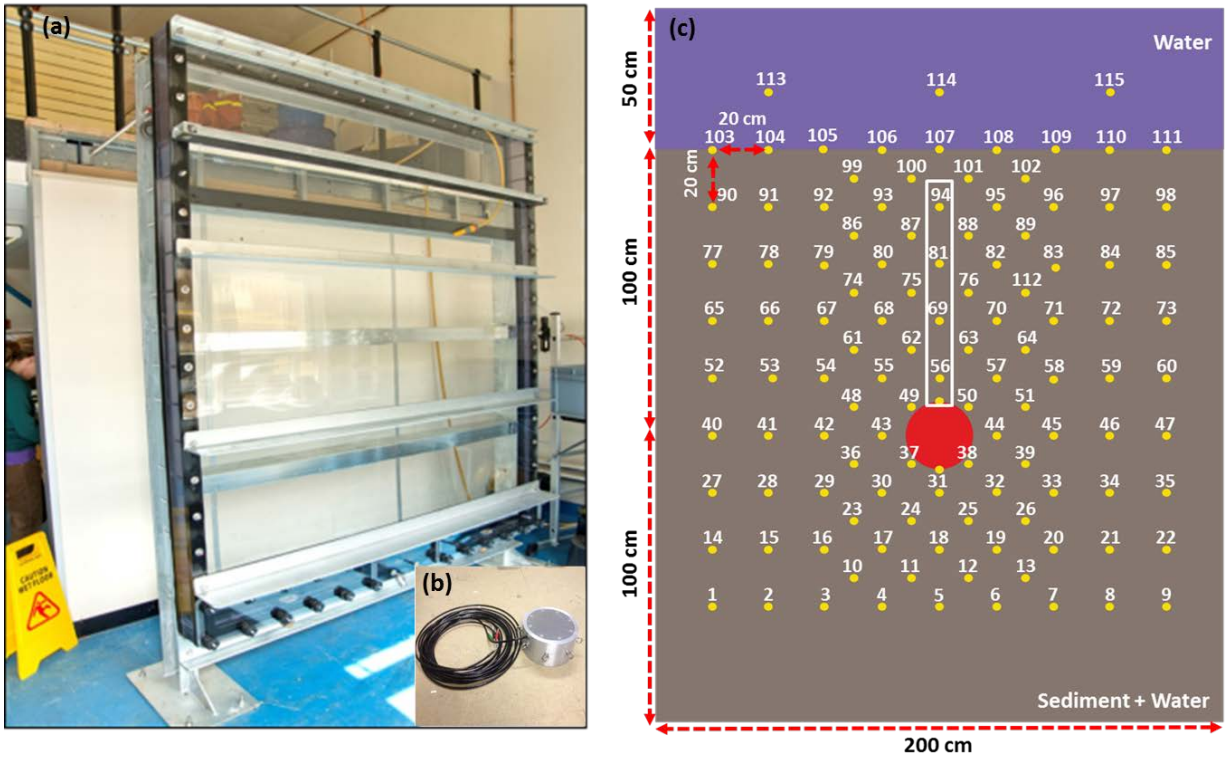

Figure 1: (a) Photograph of the 2D experimental tank, (b) aluminium heat source (22 cm diameter) and (c) a schematic diagram showing the TC grid locations. The temperature measurements from the TC attached on the heat source (TC 116) and those located vertically above it (inside the marked white box) were used to assess attainment of steady state temperature distribution of each experiment.

Table 1: Ballotini sediment properties for the three different size classes

Ballotini materials	Grain size range	Grain size, d_m (m)	Porosity range, n	Permeability range, k (m^2)
Low Permeability Class	Lower	32×10^{-6}	0.15	2.66×10^{-14}
	Mean	45×10^{-6}	0.2	1.41×10^{-13}
	Upper	58×10^{-6}	0.25	5.19×10^{-13}
Medium Permeability Class	Lower	150×10^{-6}	0.26	4.01×10^{-12}
	Mean	200×10^{-6}	0.32	1.57×10^{-11}
	Upper	250×10^{-6}	0.38	5.0×10^{-11}
High Permeability Class	Lower	1000×10^{-6}	0.35	5.64×10^{-10}
	Mean	1230×10^{-6}	0.4	1.49×10^{-09}
	Upper	1400×10^{-6}	0.45	3.28×10^{-09}

2.2. Achieving steady state thermal distribution

For each experiment, we ensure that a steady state thermal distribution has been reached by calculating temperature change with time. Examples of this approach using the very coarse sand sample with a permeability of $1.41 \times 10^{-9} m^2$ are shown in Figure 2a and 2b for experiments with surface temperatures of 7ºC and 18ºC above ambient respectively. Figure 2 is based on the TC temperature measurements attached directly to the top of the heat source (TC116) and within the surrounding sediments; from the nearest (TC56 – 11.7cm from TC116) to the most distally heated TC located vertically above the heat source (TC94 – 69.9 cm from TC116). The experiments with surface temperature 7ºC and 18ºC above ambient, achieved steady state after 7200 (5 days) and 2448 minutes (1.7 days) respectively (Figure 2). Similar assessments were made for all experiments undertaken to ensure equilibrium had been achieved.

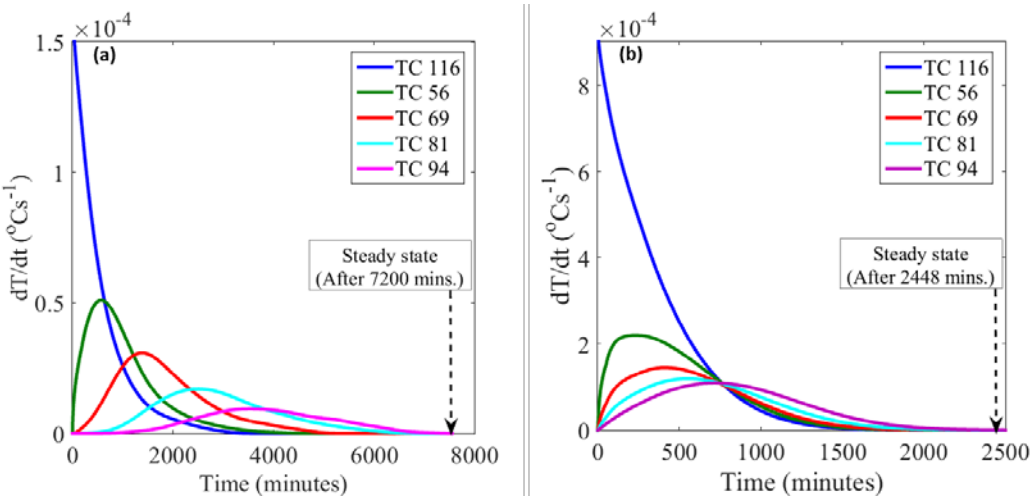

Figure 2: The rate of change in temperature ($\partial T/\partial t$) plot shows attainment of steady state at zero $\partial T/\partial t$ for the heat flow through the high permeability (10^{-9} m^2) very coarse sand sediment with temperatures of 7 ^oC (a) and 18 ^oC (b) above ambient.

2.3. Temperature data measurement reproducibility

The reproducibility of the temperature time series data has been tested through two replicate experiments, A and B (Figure 3), using the fine sand sized sample at steady state. TC9 (i.e. bottom right hand corner of the tank) shows a temperature that is the most stable throughout the run (Figure 3a) with less change than either the ambient air temperature (TC119) or the temperature of the water above the sediment interface (TC114). With the same power input, the measured surface temperatures of the heat source (TC116) were 37.9^{o}C and 34.8^{o}C with ambient sediment temperature (TC9) of 19.3^{o}C and 16.0^{o}C respectively. The two experiments show the same pattern of temperatures (Figure 3b), but a 2.9 ± 0.4^{o}C mean difference from all sediment TCs at steady-state. When all temperatures are corrected to be relative to TC9, the mean offset between the two experiments is 0.4 ± 0.4^{o}C (Figure 3c). Consequently, we report all measurements as the temperature above ambient sediment temperature, as recorded at TC9 at the steady state time step. Comparing the temperature measurements at each time step of the

two experiments from the 100 sediment TCs gives a high correlation coefficient (R^2) of 0.97 which is significant at the 95% confidence limit and with a T-statistic of 3.60 x 10^3 and P-value of zero (Figure 3d). The points on the scatter plot are coloured based on the density variation of the clustered points.

We also generated 2D time dependent heat flow surfaces based on linear interpolation of the neighbouring temperature distributions measured at each TC location for each replica experiment after correction (Figure 3e-3f). This further visually confirms reproducibility between experiments.

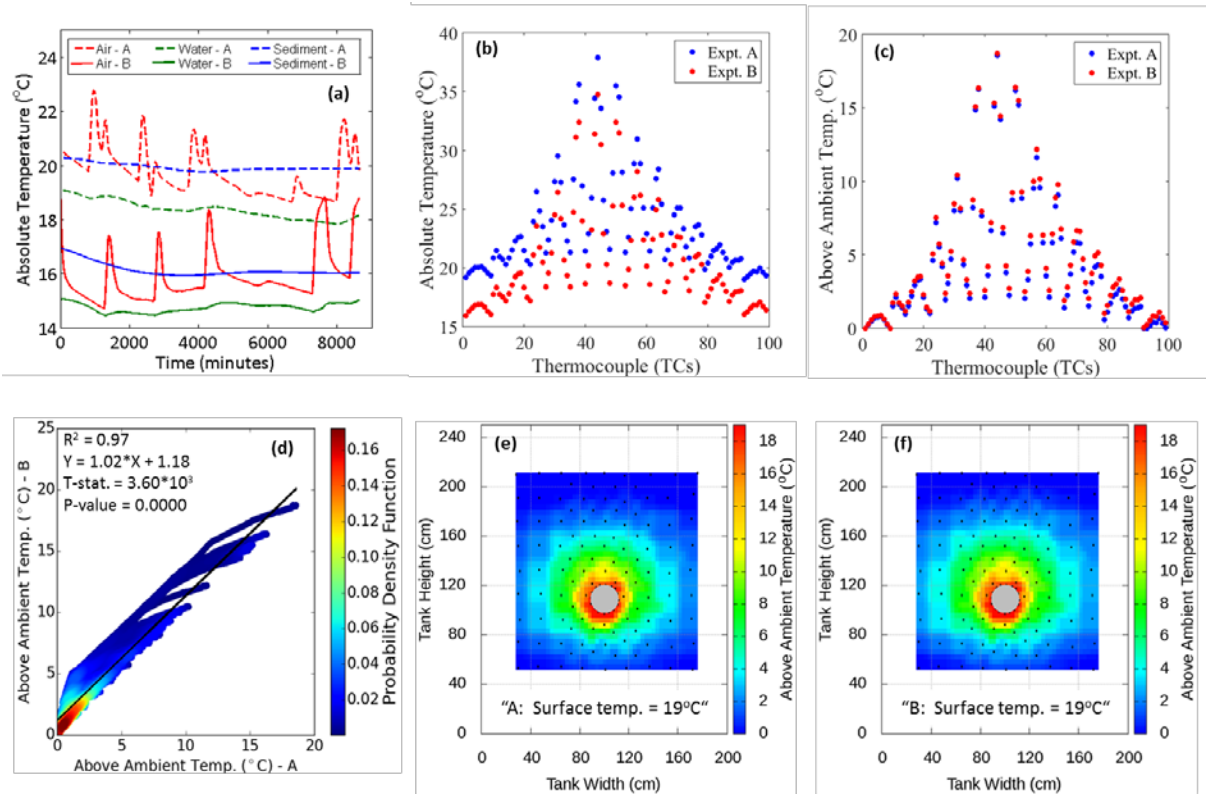

Figure 3: Assessment of the data measurement reproducibility using two replicate experiments A and B with steady state skin temperature (TC116) of 37.9 ^oC and 34.8 ^oC with ambient sediment temperature (TC9) of 19.3 ^oC and 16.0 ^oC respectively. Panel (a) represents the ambient air, water and sediment temperature; (b) and (c) are the steady state temperature

distributions before and after correction respectively; (d) cross-plot of the 864000 temperature measurements from the two replicate experiments; and (e) and (f) are the steady state 2D heat flow surfaces after correction for the two replicate experiments with heat source surface temperature 19 ^{o}C above ambient.

3. RESULTS

A total of fourteen heat flow experiments have been conducted to investigate the thermal regimes generated from typical cable surface temperatures within low, medium and high permeability sediments, to cover a range representative of the continental shelf. Normalised heat flow surfaces and radial temperature distributions were used to determine whether the heat transfer mode from a cable buried in such sediments is dominated by conduction or convection.

Finite Element Method (FEM) simulations have also been undertaken to model the steady state heat transfer within the tank experiment from the heat source flowing through the surrounding ballotini sediments. The construction of the model is based on the procedure described in Hughes et al. (2015), but has been modified to use the input parameters of the tank experiment. This included altering the model geometry to mimic the tank dimensions, and a constant temperature boundary condition being imposed at the surface of the simulated heat source. Thus, each heat flow experiment is compared with corresponding numerical simulation results using the same heat source surface temperatures and surrounding sediments properties of the low permeability mean class, medium permeability upper class and high permeability mean class (Table 1).

3.1. Thermal regime at low permeability

The steady state temperature distributions within the low permeability sediment have been acquired from four experimental runs with heat source surface temperatures of 10, 18, 45 and 60^{o}C above ambient. They all show radially symmetrical temperature distributions centred on the heat source, for surface temperatures of 10^{o}C (Figure 4a) to 60^{o}C (Figure 4c) above ambient measured at TC9. At the highest heat source temperature of 60^{o}C (Figure 4c), there is a >10 ^{o}C temperature rise in the surrounding sediments up to 40 cm from the heat source.

Figure (4a' to 4c') shows the FEM model runs completed for each low permeability case with varying heat source temperature and further shows radially symmetrical temperature distributions centred on the heat source, for surface temperatures of 10^{o}C (Figure 4a'), 18^{o}C (Figure 4b') and 60^{o}C (Figure 4c') above ambient. This heat flow pattern are highly comparable with the thermal regimes demonstrated with the lab experimental data (Figure 4a to 4c) within low permeability sediments. The heating effect to the surrounding sediment is also comparable for the lower heat source temperatures (Figure 4a and 4b), but as the temperature reaches 60^{o}C (Figure 4c and 4c'), the disparity is due to remnant heat loss to the sides of the experimental tank after insulation. Thus for the numerical simulation result (Figure 4c'), at 60^{o}C there is a >10 ^{o}C temperature rise in the surrounding sediments up to 60 cm from the heat source.

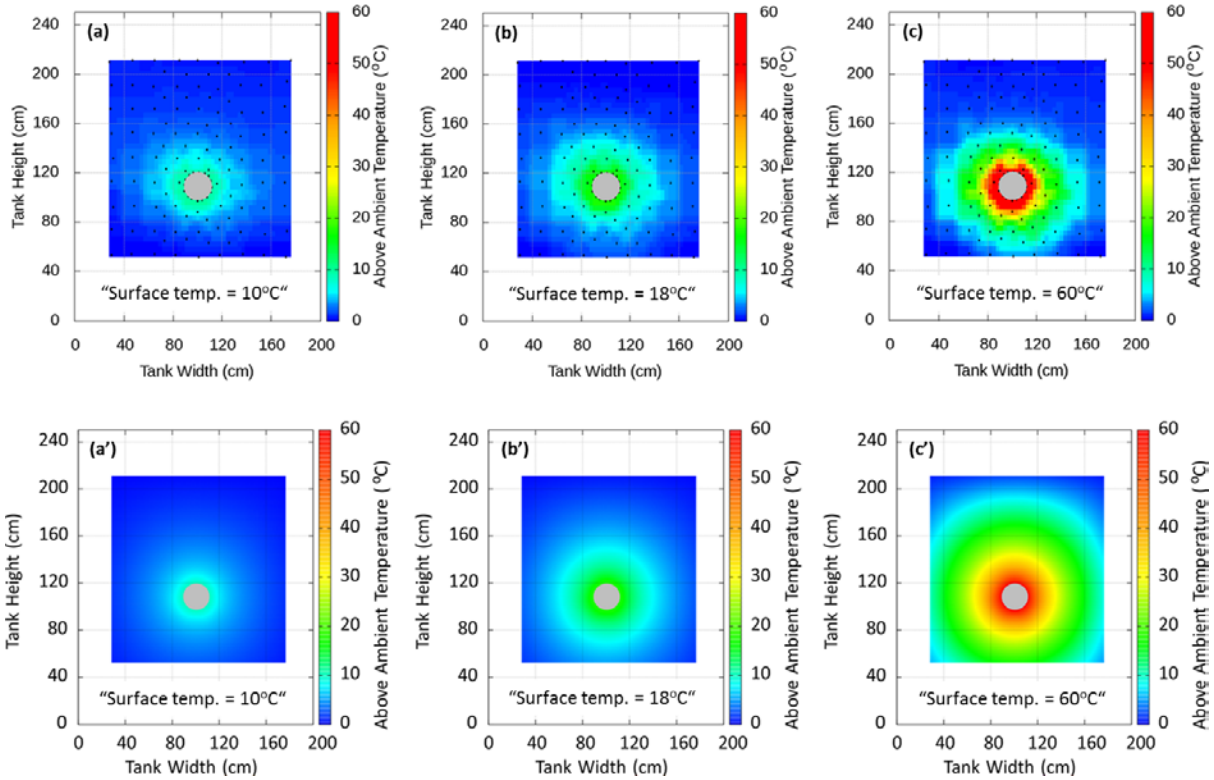

Figure 4: Steady state temperature distributions for low permeability (1.41 x 10^{-13} m^2) sediments with 10°C, 18 °C and 60 °C above ambient cable surface temperatures from the lab experiments (a, b and c) and corresponding numerical simulation results (a', b' and c').

3.2. Thermal regime with medium permeability

The steady state temperature distributions within the medium permeability sediment from six experiments is driven by heat source surface temperatures of 10, 19, 36, 43, 51 and 55°C above ambient respectively. The temperature is centred on the heat source for skin temperatures of less than 10°C above ambient (Figure 5a), but is increasingly asymmetric as the skin temperature increases (Figures 5b-5d). At skin surface temperatures of >19°C there is a temperature increase >10°C at 40 cm radius from the heat source (Figure 5b); vertically above the heat source this 10°C increase reaches 100 cm at a heat source surface temperature of 55°C (Figure 5d). Also, at the highest heat source temperature (55°C – Figure 5d) the shallowest 20

cm of the sediment experiences an increase in temperature of up to 20^{o}C over a zone about 60 cm wide.

Figure (5a'-5d') shows the FEM simulations for the medium permeability case with varying heat source temperature. Again at 10^{o}C (Figure 5a'), the modelled thermal regime shows radially symmetrical temperature distributions centred on the heat source, however as the temperature exceeds 19^{o}C (Figure 5b') an asymmetric heat flow pattern starts to develop and progresses with increasing heat source temperature (Figure 5b'-5d'); similar to the lab experimental results (Figure 5a-5d). The heating effect to the surrounding sediment is also comparable for lower and higher heat source temperatures (Figure 5a-5b) because with increasing source temperature, asymmetric vertically upwards heat flow pattern develops with negligible impact of the remnant heat loss to the sides of the experimental tank after insulation.

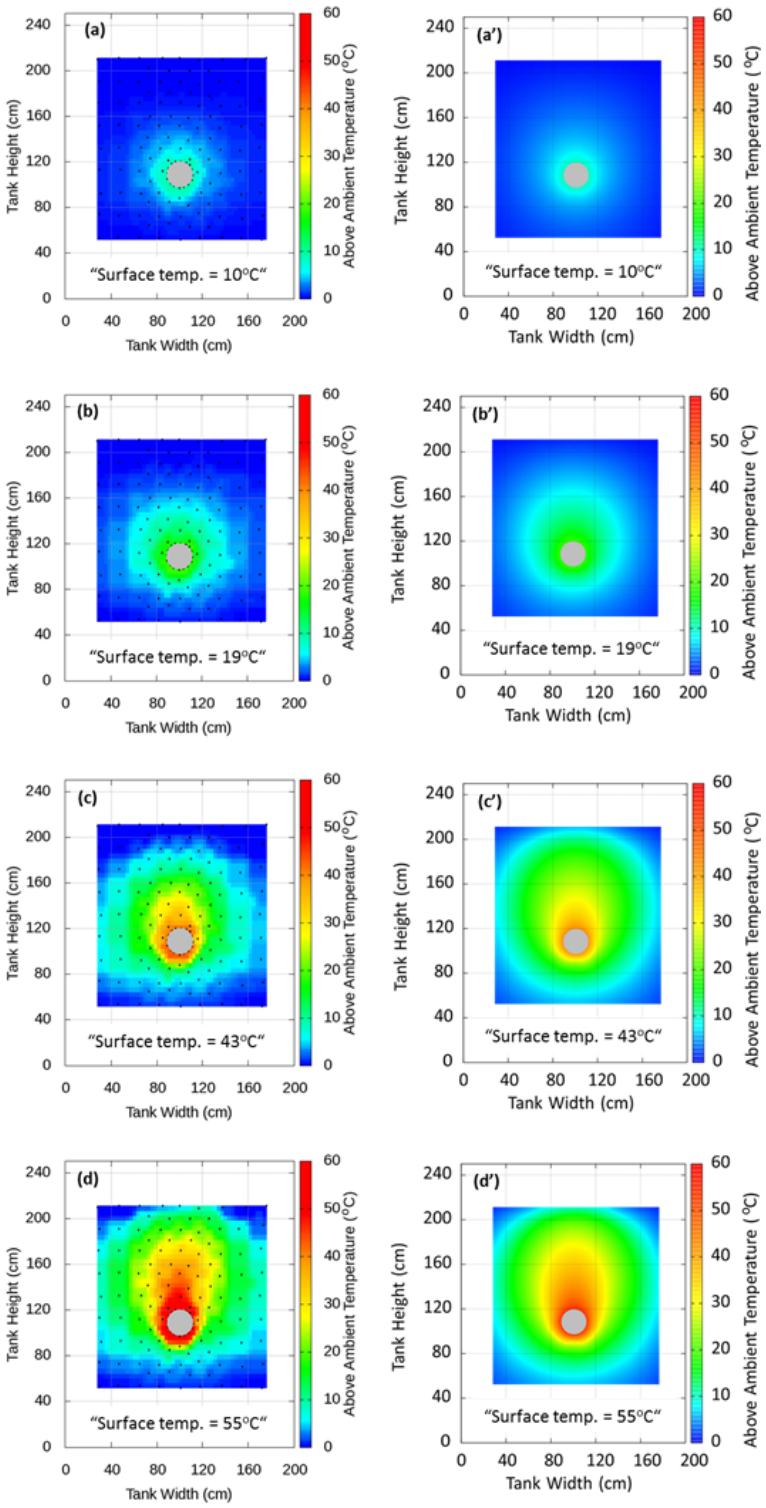

Figure 5: Steady state temperature distributions for medium permeability (5.0 x 10^{-11} m^2) sediments with 10°C, 19 °C, 43 °C and 55 °C above ambient cable surface temperatures from the lab experiments (a, b, c and d) and corresponding numerical simulation results (a', b', c' and d').

3.3. Thermal regime at high permeability

The steady state temperature distributions within the high permeability very coarse sand sediment are recorded for four experiments with heat source surface temperatures of 7, 9, 14 and 18^{o}C above ambient. They all show temperature distributions that are highly asymmetric, even at the lowest input surface temperature of 7^{o}C above ambient (Figure 6a). At these initial temperature inputs, the generated thermal plume has a width up to 140 cm for a 7^{o}C rise above ambient, narrowing to 100 cm, 80 cm and 60 cm as the heat source surface temperature is increased to 9, 14 and 18^{o}C above ambient respectively.

The FEM heat flow simulation results for the high permeability case (Figure 6a' to 6c') are also comparable with the lab experimental results, as all the thermal regimes demonstrate highly asymmetric patterns even at the lowest heat source temperature run of 7^{o}C above ambient (Figure 6a'). The heating effect of the vertical heat plume to the surrounding sediments are relatively broader for the observed results (Figure 6a to 6c), due to remnant heat loss to the sides of the experimental tank after insulation.

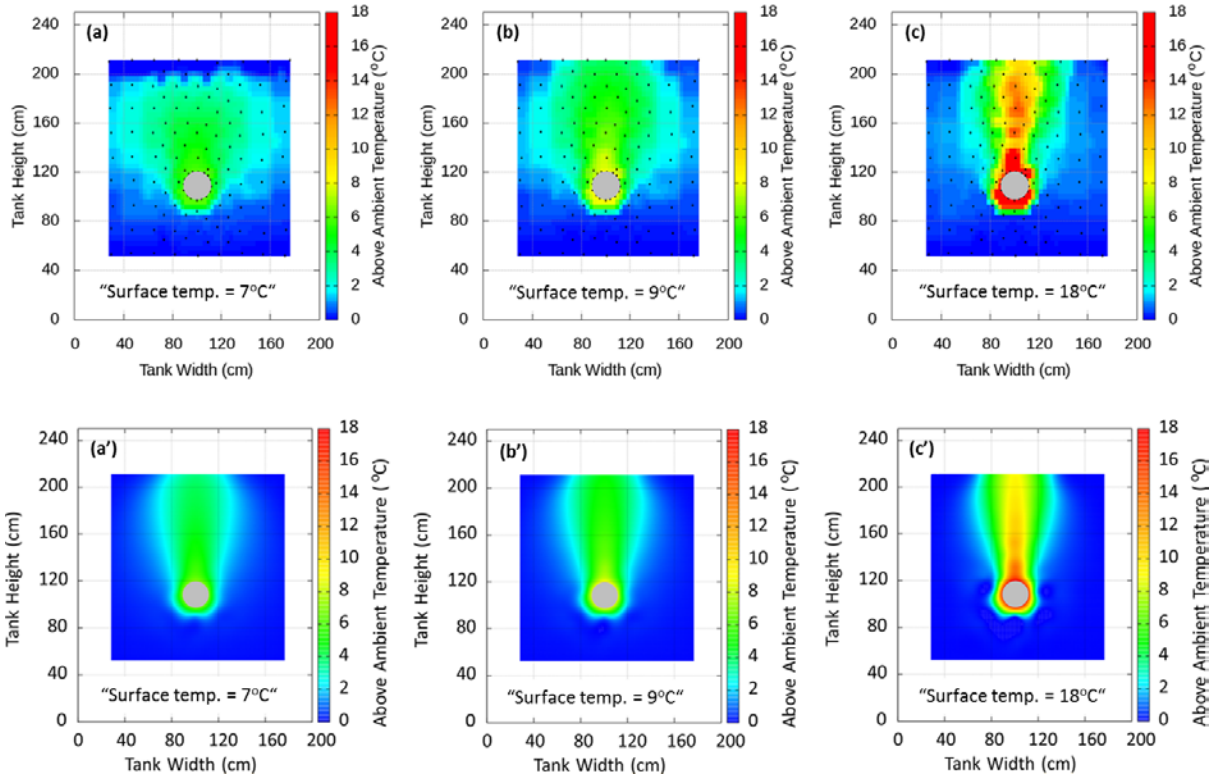

Figure 6: Steady state temperature distributions for high permeability (1.49 x 10^{-9} m^2) sediments with 7°C, 9 °C and 18 °C above ambient cable surface temperatures from the lab experiments (a, b and c) and corresponding numerical simulation results (a', b' and c').

4. DISCUSSION

4.1. Comparing the different thermal regimes

To allow comparison of the temperature distributions between the steady state runs that are not affected by the different temperatures at the heat source or the variations in ambient conditions in the laboratory (i.e. characterize only the shape of the distribution rather than absolute values), normalized difference surfaces are generated using Figure 4c with a radial heat flow pattern at 60°C above ambient temperature difference as reference in all cases. For example for the 10°C (Figure 5a) above ambient surface temperature experiment ($Nor.Diff_{10}$):

$$Nor.Diff_{10} = \frac{T_{10} - T_{a_{10}}}{T_{m_{10}} - T_{a_{10}}} - \frac{T_{60} - T_{a_{60}}}{T_{m_{60}} - T_{a_{60}}} \quad (2)$$

Where T, T_a , T_m are the observed TC, ambient, and maximum surface temperatures at steady state, and the additional suffix gives the temperature difference from ambient.

Thus, a normalized difference of zero implies that the shape of the temperature distribution is the same as the reference (Figure 4c), but not that the absolute temperatures, or the temperature increases above ambient, are the same. Normalised temperatures are close to zero (Figure 7a) within the low permeability sediments even up to 60 ^{o}C above ambient and also for the medium permeability sediments with skin temperatures up to 10 ^{o}C above ambient. However, within the medium permeability experiments, as the skin temperature increases above 19^{o}C, an area of small positive normalised temperature difference is observed above the heat source (Figure 7b). This becomes progressively larger in magnitude and extent as the temperature difference increases further (Figure 7c-7d), extending up to 80 cm above the source with a 55 ^{o}C skin temperature (Figure 7d). Within the high permeability sediments, even a 9^{o}C skin temperature leads to a high positive normalised temperature extending beyond 100 cm above the source while relatively small negative normalise difference develops up to 20 cm below and either sides of the source (Figure 7e-7f).

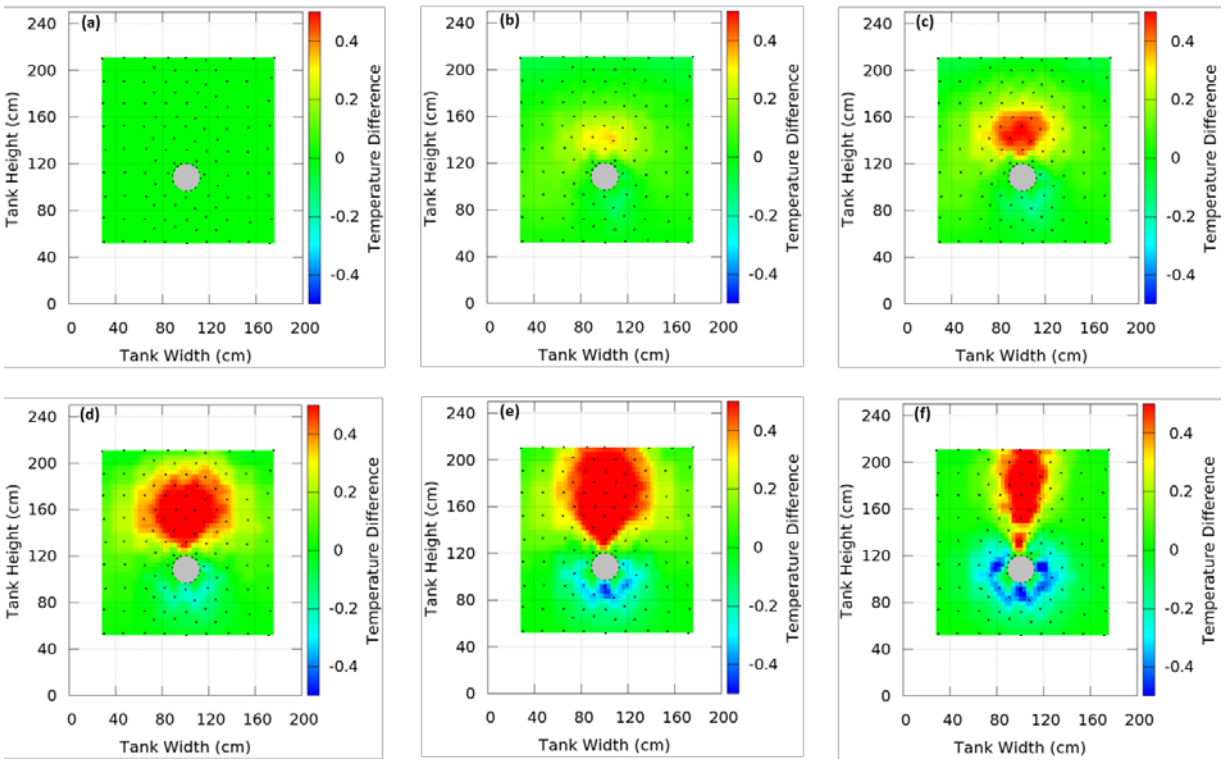

Figure 7: Normalised difference surfaces of the steady state temperature within: (a) low permeability (1.41 x 10^{-13} m^2) sediment with 45 ^oC above ambient skin temperature; (b), (c) and (d) medium permeability (5.0 x 10^{-11} m^2) sediment with skin temperature 36 ^oC, 43 ^oC, 55 ^oC above ambient respectively; and (e), (f) high permeability (1.49 x 10^{-9} m^2) sediment with skin temperature 9 ^oC, 18 ^oC above ambient cable surface temperature respectively.

4.2. Mode of heat transfer

The temperature distribution around a line source in homogeneous sediments is expected to be approximately radial if heat transfer is occurring by conduction (Carslaw and Jaeger, 1959, Turcotte and Schubert, 2002). All points on radial distance plot of temperature should fall along a radial curve for steady state conductive heat flow with negligible heat generation. However, at the onset of a convective heat flow, the points on the radial plots begin to scatter. Thus, the transition from conductive to convective heat transfer as a function of cable surface temperature

and permeability are assessed statistically from the degree of scatter in the data and depicted by the histogram line plot of the standard deviation (Figure 11) of points as a function of surface temperature against 10cm bins of radial distance starting from the heat source surface.

For the low permeability thermal regimes, radial symmetry is clearly demonstrated by plotting the observed TC temperature against the radial distance of each TC away from the center of the internal heat source (Figure 8a to 8c). There is less than 4^{o}C temperature variation at any radial distance from the source, with high temperatures at the source and essentially ambient conditions at the furthest distances. The average standard deviation histograms of the binned radial scatter points with varying surface temperatures ranges from 0.03 to 0.05 (Figure 11a). Also the radial point plots (Figure 8a' to 8c') extracted from the FEM heat flow simulation shows radial symmetry with 0.03 average standard deviation and overlapped histogram plots for all temperatures (Figure 11a') that are comparable with the corresponding lab results.

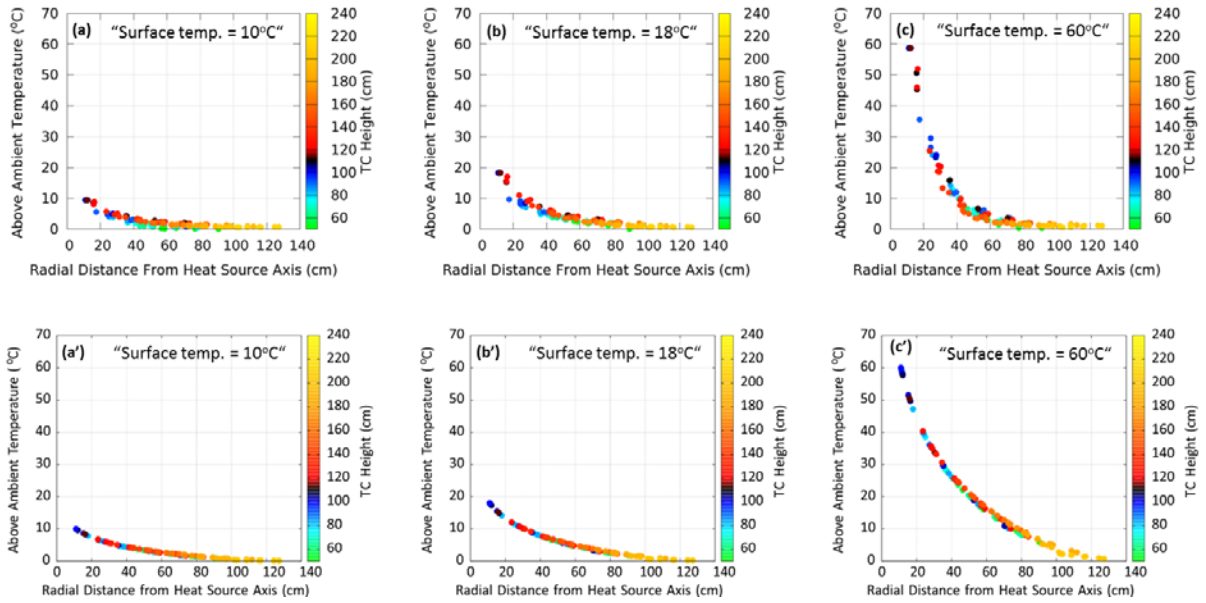

Figure 8: Radial steady state temperature distributions within low permeability (1.41 x 10^{-13} m^2) sediments with 10°C, 18 °C and 60 °C above ambient cable surface temperatures from the lab experiments (a, b and c) and corresponding numerical simulation results (a', b', c').

The observed thermal regimes within the medium permeability sediments (Figure 5), shows that at 10°C above ambient surface temperature, the temperature distribution is primarily radial with less than 4°C temperature range at any single distance from the source (Figure 9a). However, with increasing heat source temperatures this pattern changes as the range of temperature measurements at any single radial distance increases significantly (Figure 9b-9d), reaching 40°C at the highest surface temperature used (55°C: Figure 9d). TCs below the heat source (110cm height) show a similar temperature variation with distance irrespective of the temperature of the heat source. However, above the heat source, the spread in TC values is in response to the well-developed thermal plume (Figure 5c-5d). At 10°C heat source temperature, the standard deviation histogram of the binned radial scatter points shows a similar pattern to the low permeability case with an average value of 0.05. However, as the temperature increases from 19°C to 55°C, the average value of the standard deviation histogram increases further;

ranging from 0.6 to 1.5 respectively (Figure 11b). The critical (average) standard deviation per surface temperature value is 0.06 (representing the onset of radial asymmetric pattern) and it is the average degree of scatter with 19 ^{0}C (Figure 9b and 9b'). For the FEM heat flow simulations, the extracted radial point plots (Figure 9a' to 9d') shows radial symmetry at 10^{o}C heat source temperature with an onset of radial asymmetric pattern as the surface temperature exceeds 19^{o}C (Figure 9b'). Thus, the radial scatter points and standard deviation histogram plots (Figure 11b') from FEM models are comparable with the corresponding lab experiment results.

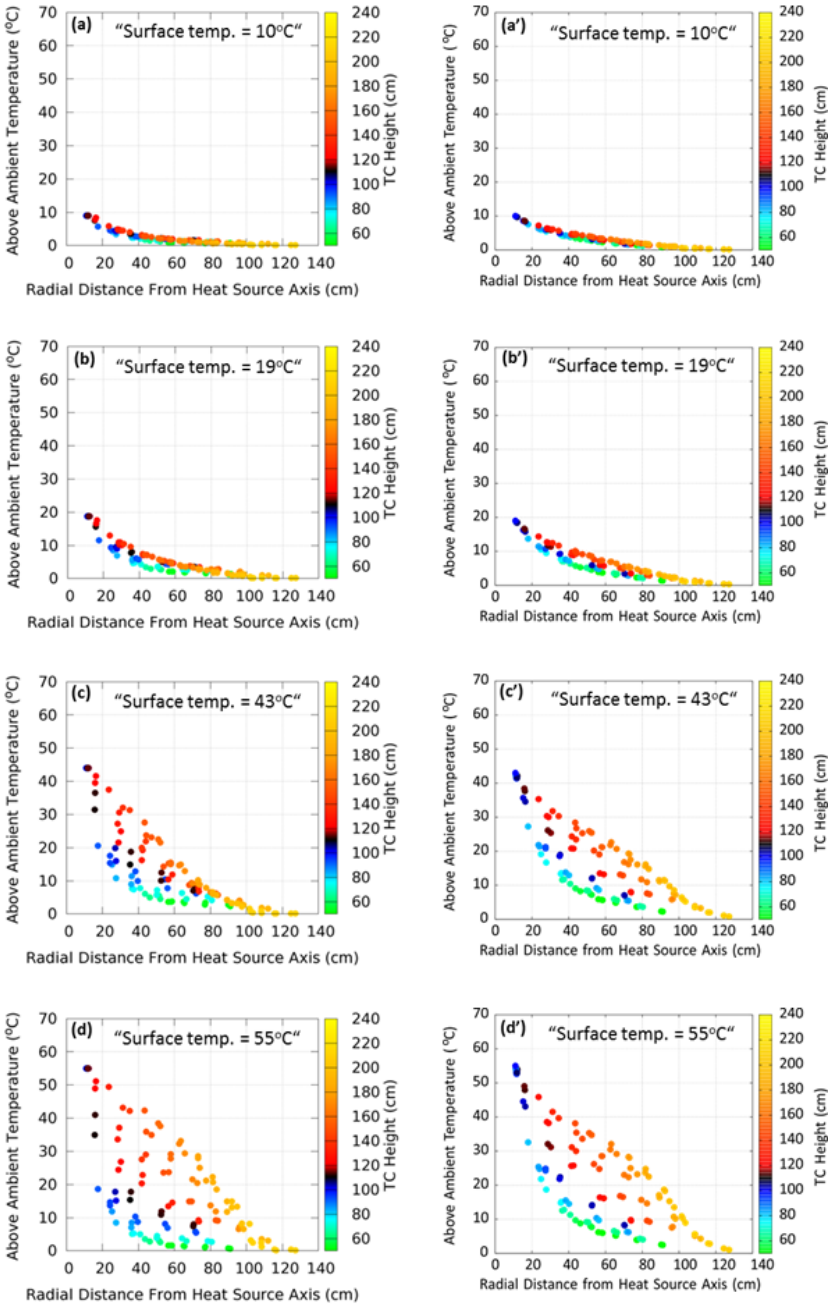

Figure 9: Radial steady state temperature distributions within medium permeability (5.0 x 10^{-11} m^2) sediments with 10 °C, 19 °C, 43 °C and 55 °C above ambient cable surface temperatures from the lab experiments (a, b, c and d) and corresponding numerical simulation results (a', b', c' and d').

For the observed high permeability thermal regimes, the plot of TC temperature against the radial distance from the heat sources (Figure 10a-10c), shows a broad spread of temperatures at each radial distance increasing from 6°C with a skin temperature of 7°C above ambient to 18°C with a skin temperature of 18°C above ambient. The highest temperatures are recorded at the TCs above the heat source, and the TCs below the heat source remain essentially at ambient conditions. The average standard deviation histograms of the binned radial scatter points with varying surface temperatures ranges from 0.19 to 0.23 (Figure 11c). The radial point plots (Figure 10a' to 10c') extracted from the FEM heat flow simulation, also shows radial asymmetric pattern with an average standard deviation histogram plots (Figure 11c') that are comparable with the corresponding lab results (Figure 11c).

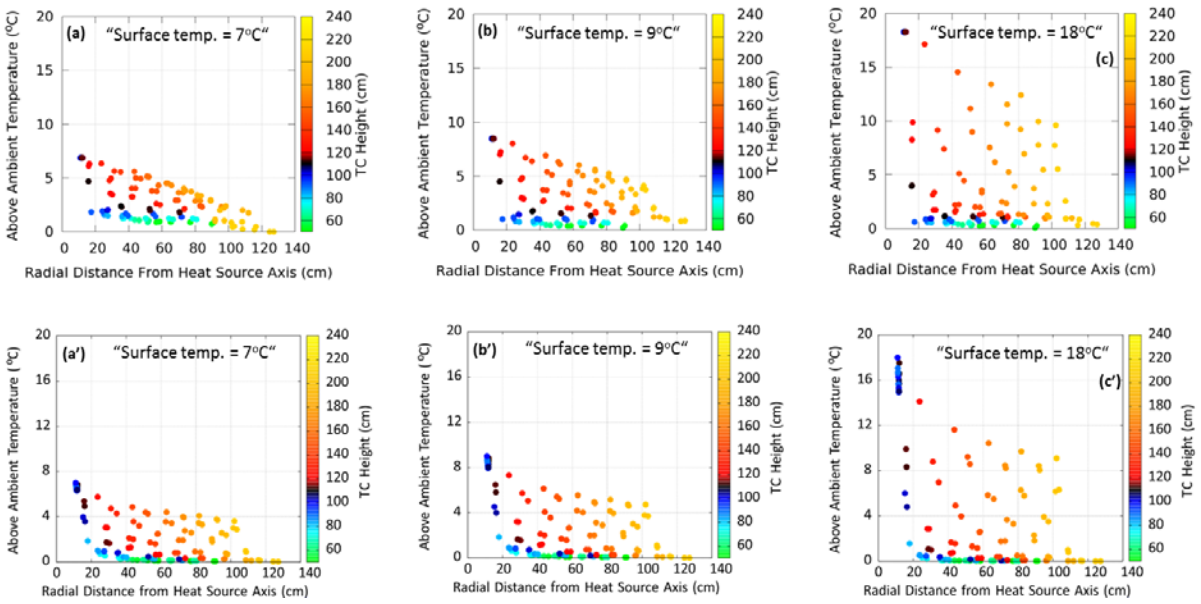

Figure 10: Radial steady state temperature distributions within high permeability (1.49 x 10^{-9} m^2) sediments with 7 °C, 9 °C and 18 °C above ambient cable surface temperatures from the lab experiments (a, b and c) and corresponding numerical simulation results (a', b', c').

Thus, the radial temperature distribution in our experiments suggests that the primary mode of heat transfer is conductive within the low permeability sediments irrespective of the heat source surface temperature (Figure 4 and 8) as well as conductive within the medium permeability sediments for heat source surface temperatures below 10^{o}C above ambient (Figure 5a, 5a', 7a, 9a and 9a'). Conversely, the increasing non-radial component temperature distribution within the medium permeability sediments with 19^{o}C above ambient temperature, suggests the onset of convective heat transport (Figure 5b, 5b', 7b, 9b and 9b'). The temperature distribution within the high permeability sediments is not radially symmetric even at 7^{o}C above ambient temperature, suggesting a convective heat transfer mode (Figure 6, 7e-7f and 10).

Figure 12 shows the transition curve line for the onset of convective heat transfer and the space of cable surface temperature and permeability that leads to conductive and convective heat transfer. All points with varying cable surface temperatures for permeabilities 1.41 x 10^{-13} m^2, 5.0 x 10^{-11} m^2 and 1.49 x 10^{-9} m^2 are overlapped points from both lab experiments and FEM heat flow simulations results. The additional result points along permeabilities 1.0 x 10^{-12} m^2, 1.67 x 10^{-11} m^2 and 1.0 x 10^{-10} m^2 with varying cable surface temperatures are only from FEM heat flow simulation results presented in the supplementary information S1 Figure 1, 2, 3 and 4.

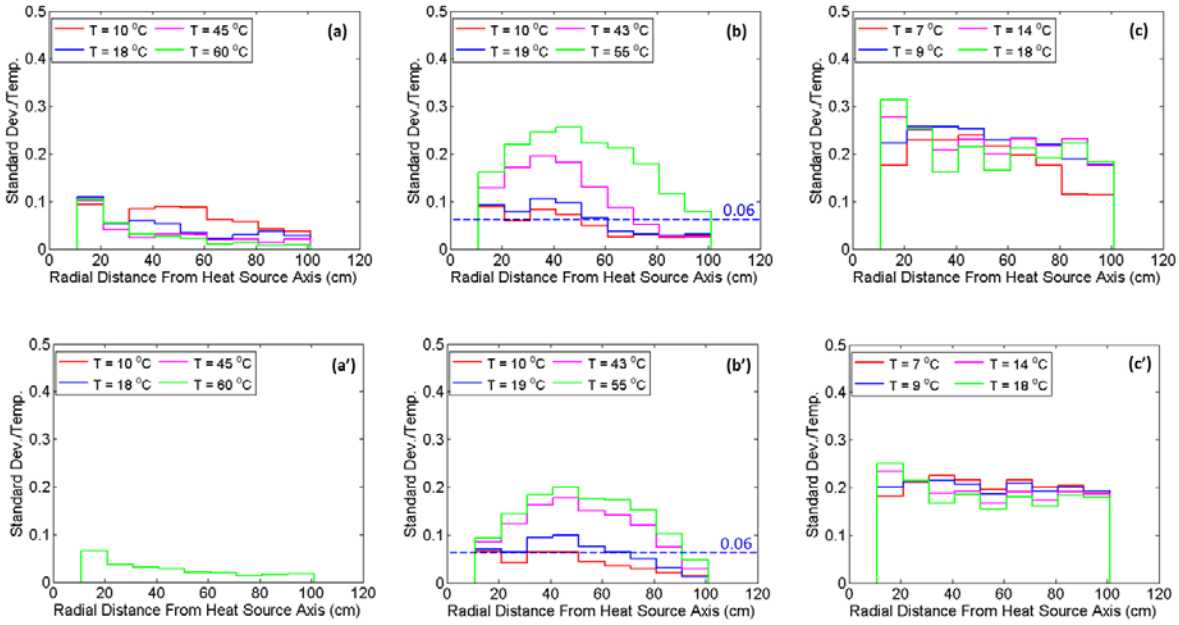

Figure 11: The standard deviation histograms of 10cm binned radial scatter points with varying surface temperatures within low, medium and high permeability sediments from the lab experiments (a, b and c) and corresponding numerical simulation results (a', b', c'). The critical (average) standard deviation per surface temperature value is 0.06 (horizontal dash blue line) which represent the onset of radial asymmetric pattern and transition from conductive to convective heat transfer.

Further, the increase of temperature above the heat source (Figures 7d-7f) is consistent with our interpretation of significant convective heat transport component, with pore fluid being heated around the source and rising vertically. The ambient temperatures recorded below the heat source show the convective recharge. This transition from conductive to convective heat transport is consistent with the predictions of the modelling approach of Hughes et al. (2015).

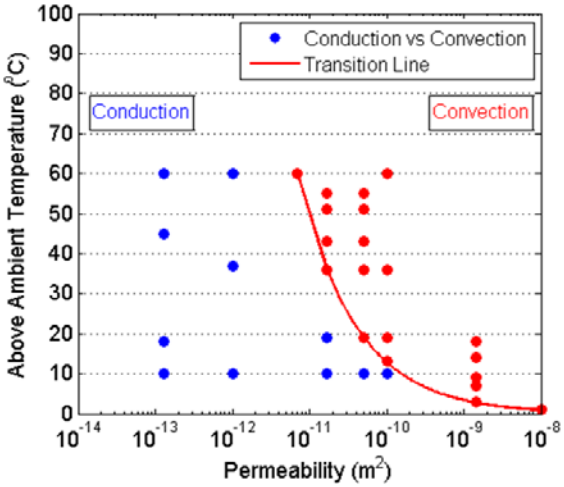

Figure 12: Plot of cable surface temperature against permeability of the surrounding Ballotini sediments, showing the onset of convective heat transfer (transition curve line) and the space of cable surface temperature and permeability that leads to conductive and convective heat transfer.

4.3. Implications for environments around submarine HV cables

Our results show that in the conductive examples (low permeability sediments, Figure 4c, and medium permeability sediments with low skin temperatures, Figure 5a) sediment temperature increases of more than 10°C are limited to within less than a 40 cm radius of the heat source. However, in the convective heat transport regimes sediment can be heated by more than 10°C at significantly greater distances above the cable. In medium permeability sediment, as the skin temperature increases beyond 19°C, the heating extends beyond 40cm (Figure 5b) and increases to 100 cm as the skin temperature reaches 55°C (Figure 5d). Furthermore, within high permeability sediments, the convective heating effect of at least 9°C (Figure 6b) extends vertically beyond the typical 100 cm burial depth of submarine HV cables.

Thus, with regards to the environmental regulations of the German Federal Maritime and Hydrographic Agency (BSH) acceptable limit of < 2 K (2 ^{o}C) above ambient temperature rise at 20 cm below the seabed (BSH, 2014), our results clearly shows 2^{o}C temperature rise below the 20 cm depth line for conductive thermal regimes even for skin temperatures of 60^{o}C above ambient (Figure 13a-13b). However, the 2^{o}C temperature rise is above the 20 cm depth line for strongly convective thermal regimes even at 7^{o}C above ambient heat source skin temperature (Figure 13c-13d).

Furthermore, temperature is an important and long recognised environmental factor in the ecosystems of benthic biota (benthic communities and those living in the top 20 cm sub-seafloor). In particular, the convective thermal regime with observed above ambient temperature increase of between 5 and 14^{o}C in the top 20 cm (Figure 13c-13d) can impact the evolutionary, physiological and behavioural responses of benthic biota as well as impact their geographical distribution over both the short and long-term (Price *et al.*, 1979, Southward and Southward, 1988, Holt, 1990, Hiscock *et al.*, 2004). Species that cannot withstand and adapt to these high surrounding thermal regimes could diminish in abundance, become extinct or migrate to colder environments (Price *et al.*, 1979, Hiscock *et al.*, 2004).

The stability of the installed buried cable could be impacted by the geotechnical properties of the seabed and these properties may be significantly changed, both during installation as well as post-installation operation (SP-Transmission and NationalGrid, 2011). With external cable surface temperatures approaching 70°C (Swaffield *et al.*, 2008, Hughes *et al.*, 2015), the surrounding host seawater-saturated sediments will endure excessive thermal conditions. Consequently, in the short term, these excessive sediment temperatures could initiate significant pore-water convection (typical to Figure 13c-13d), movement of individual grains, reduction of bed shear stress (and fluidization), enhanced erodibility and seabed scour; leading to possible cable exposure and damage by ship anchor and fishing gear. In the medium

to long term, the temperature changes could cause changes in pore water and solid phase geochemistry including: degradation of solid organic matter, recrystallization and dehydration of clay minerals, mobilization of potentially toxic metals and precipitation of calcium carbonate.

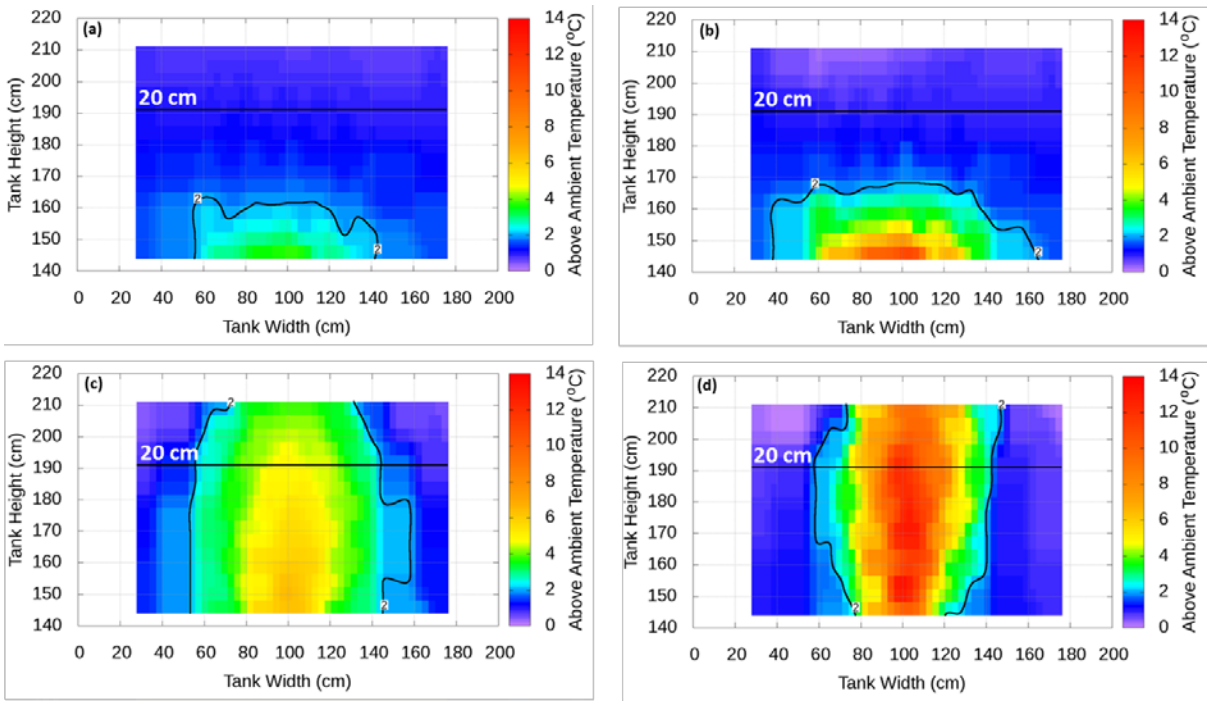

Figure 13: Steady state temperature surfaces for the upper 80cm of the sediments showing the 20 cm depth mark and 2 °C contour typical for: (a), (b) low permeability (1.41 x 10^{-13} m^2) conductive thermal regimes with skin temperature 18 °C and 60 °C above ambient respectively; and (c), (d) high permeability (1.49 x 10^{-9} m^2) convective thermal regimes with skin temperatures 9 °C and 18 °C above ambient respectively.

4.4. Implications for cable rating and ampacity

Our results show the varied thermal regimes associated with submarine HV cables buried in different substrates, and conditions for occurrence of both conductive and convective heat transfer modes. Cable ampacity ratings are based on the ability to transfer heat generated by the cable into the surrounding environment. Excessive temperatures within the cable insulation would lead to premature cable degradation and potentially failure. Convective heat transport is significantly more efficient than conductive, so that the same heat transport produces a lower cable temperature (e.g., Hughes et al., 2015) due to the constant pore fluid recharge (Figure 8e-8f). Since the transition between conduction-dominated and convection-dominated heat transport occurs within the ranges of sediment commonly found on continental shelves, the basic assumptions of isothermal ground temperature, homogeneous burial sediment and only conductive heat transfer as contained in the IEC 60287 standard (BS-IEC-60287-1-1:2014, 2014) are not appropriate for the marine environment. Use of this standard in coarser sediments with medium to high permeabilities where convection occurs will lead to significant under-rating of submarine HV cables. Consequently, we suggest that the influence of sedimentary environments on the thermal performance of cables should be taken into account during the cable route planning phases of such infrastructure projects.

5. CONCLUSIONS

We have used temperature measurements from a specifically designed 2D laboratory experiments to demonstrate the impacts of varying sediment permeability and generated temperature on the surrounding thermal regimes experienced by submarine HV cables buried within near surface shelf sediments. Our results suggests that, for submarine HV cables with surface temperatures up to 60°C above ambient and buried within clays to coarse silts with low permeability up to ~ 10^{-13} m^2, the surrounding thermal regime and mode of heat transfer will

be dominantly conductive. Temperatures are only raised significantly within 40 cm radius of the cable. Fine sands with medium permeability ~10^{-11} m^2 are a transitional environment which is conductive at low cable surface temperatures, but becomes convective as the cable surface temperatures increase above ~20°C relative to ambient. Significantly increased temperatures are observed up to 1 m above the cable at skin temperatures of 55°C. In very coarse sands with high permeability ~10^{-9} m^2 convective heat transfer occurs even at skin temperatures as low as 9°C above ambient, and the fluid remains hot over distances exceeding the typical 100 cm burial depth of submarine HV cables. These results are supported by the FEM model results run following the approach of Hughes et al. (2015). While widespread convective heat transport would increase cable ampacity ratings, it could also cause problems with existing environmental regulations which are based solely on temperature changes at a specific depth in the sediment.

ACKNOWLEDGEMENTS

This research was funded by National Grid UK Limited, UK Engineering & Physical Sciences Research Council (EPSRC) Industrial CASE Award E73999C and the University of Southampton.

Data Policy: The raw and processed data presented in this paper is hosted via the University of Southampton Eprints site (eprints.soton.ac.uk), which will be retained for at least 10 years as per the Universities research data management policy.

REFERENCES

Amyx, J.W., Bass, D.M. & Whiting, R.L., 1960. Petroleum Reservoir Engineering: Physical properties, *McGraw-Hill, New York*, 610.

Bear, J., 1972. Dynamics of Fluids in Porous Media, *Elsevier, New York*, 166.

Beck, A.E., 1976. An improved method of computing the thermal conductivity of fluid-filled sedimentary rocks, *Geophysics*, 41, 133-144.

Blair, S.C., Berge, P.A. & Berryman, J.G., 1996. Using two-point correlation functions to characterize microgeometry and estimate permeabilities of sandstones and porous glass, *J. Geophys. Res.*, 101, 20,359-320,375.

Blott, S.J. & Pye, K., 2001. GRADISTAT: A grain size distribution and statistics package for the analysis of unconsolidated sediments, *Earth Surf Proc Land*, 26, 1237-1248.

Boehler, R., 1996. Melting temperature of the Earth's mantle and core: Earth's thermal structure, *Annual Review of Earth and Planetary Sciences*, 24(1), 15-40.

BS-IEC-60287-1-1:2014, 2014. Electric Cables - Calculation of the Current Rating - Amendment 1, *Electrotechnical Comittee: British Standards Board*.

BSH, 2014. Standard Ground Investigation for Offshore Wind Energy, *Federal Maritime and Hydrographic Agency (BSH), Hamburg and Rostock*.

Carman, P.C., 1937. Fluid flow through granular beds, *Trans. Instn. Chem. Eng.*, 15.

Carslaw, H.S. & Jaeger, J.C., 1959. Conduction of Heat in Solids, *Oxford University Press, London*.

Celotex, 2013. Celotex TA4000, Celotex Limited, Available from: http://www.celotex.co.uk/products/ta4000 (Accessed 30 September 2015).

Christie, C.H. & Nagihara, S., 2016. Geothermal gradients of the northern continental shelf of the Gulf of Mexico, *Geosphere*, 12, 26-34.

de Leon, F. & Anders, G.J., 2008. Effects of backfilling on cable ampacity analyzed with the finite element method, *IEEE Trans. Power Del.*, 23, 537-543.

EWEA, 2013. Deep Water: The next step for offshore wind energy, *The European Wind Energy Association (EWEA), Brussels*.

Folk, R.L. & Ward, W.C., 1957. Brazos River Bar: A study in the significance of grain size parameters, *J Sediment Petrol,* 27**,** 3-26.

Geohil, A.G., 2013. Geothermal energy, *Available from: http://www.mpoweruk.com/geothermal_energy.htm (Accessed 30 September 2015).*

Gernon, T.M., Gilbertson, M.A., Sparks, R.S.J. & Field, M., 2008. Gas fluidisation in an experimental tapered bed: Insights into processes in diverging volcanic conduits., *Journal of Volcanology and Geothermal Research,* 174(1-3)**,** 49-56.

Goto, S., Mizoguchi, T., Kimura, R., Kinoshita, M., Yamano, M. & Hamamoto, H., 2012. Variations in the thermal conductivities of surface sediments in the Nankai subduction zone off Tokai, central Japan, *Marine Geophysical Research,* 33**,** 269-283.

Hiscock, K., Southward, A., Tittley, I. & Hawkins, S., 2004. Effect of changing temperature on benthic marine life in Britain and Ireland, *Aquatic Conservation: Marine and Freshwater Ecosystems,* 14**,** 333-362.

Holt, R.D., 1990. The microevolutionary consequences of climate change, *Trends Ecol. Evol.* , 5**,** 311-315.

Hughes, T.J., Henstock, T.J., Pilgrim, J.A., Dix, J.K., Gernon, T.M. & Thompson, C.E.L., 2015. Effect of sediment properties on the thermal performance of submarine HV cables, *IEEE Transactions on Power Delivery,* 30**,** 2443-2450.

Jackson, D.R. & Richardson, M.D., 2001. Seasonal temperature gradients within a sandy seafloor: Implications for acoustic propagation and scattering, *Proc. Inst. Acoust. Acoust. Oceanogr.,* 23**,** 361-368.

Jackson, D.R. & Richardson, M.D., 2007. High-Frequency Seafloor Acoustics, Underwater Acoustics Series Monograph, *Springer, New York, USA.*

Kim, T.W., Cho, Y.K. & Dever, E.P., 2007. An evaluation of the thermal properties and albedo of a macrotidal flat, *Journal of Geophysical Research-Oceans,* 112.

Lovell, M.A., 1985a. Thermal-conductivities of marine-sediments, *Quarterly Journal of Engineering Geology, London,* 18**,** 437-441.

Lovell, M.A., 1985b. Thermal conductivity and permeability assessment by electrical resistivity measurements in marine-sediments, *Marine Geotechnology,* 6**,** 205-240.

Meissner, K., Bockhold, J. & Sordyl, H., 2007. Problem of cables heat - Presentation of results from Field measurements of the seabed temperature in the range of the electric cables in Danish Offshore wind farm, Nysted Wind Farm (Denmark). *in Marine Environment Symposium,* pp. 153-161, Hamburg.

Mole, P., Featherstone, J. & Winter, S., 1997. Cable Protection – Solutions Through New Installation and Burial Approaches, *Proceedings SubOptic 1997, San Francisco,* Available from: Submarine Cable Improvement Group. http://www.scig.net/ (Accessed 30 September 2015)**,** 750-757.

Nagihara, S. & Smith, M.A., 2005. Geothermal gradient and temperature of hydrogen sulfide-bearing reservoirs, Alabama continental shelf, *Aapg Bull,* 89**,** 1451-1458.

OSPAR, 2009b. Assessment of the Environmental Impacts of Cables, *Biodiversity Series***,** 19.

Potters-Ballotini, 2011. Features of Glass Beads, Potters-Ballotini Limited, Available from: http://www.pqj.co.jp/en/product/01.html (Accessed 30 September 2015)

Price, J.H., Tittley, I. & Richardson, W.D., 1979. The distribution of Padina pavonica. (L.) Lamour. (Phaeophyta: Dictyotales) on British and adjacent European shores., *Bulletin of the British Museum Natural History Botany,* 7**,** 1-67.

Quiblier, J.A., 1984. A new three-dimensional modeling technique for studying porous media, *J. Colloid Interface Sci.,* 98**,** 84-102.

Railing, B.D., Miller, J.J., Steckley, P., Moreau, G., Bard, P., Ronström, L. & Lindberg, J., 2004. Cross sound cable project—second generation VSC technology for HVDC. *in Cigré conference*, Paris, France.

Southward, A.J. & Southward, E.C., 1988. Disappearance of the warm-water hermit crab Clibanarius erythropus from south-west Britain, *Journal of the Marine Biological Association of the United Kingdom,* 69**,** 409-412.

SP-Transmission & NationalGrid, 2011. Western HVDC Link: Preparing our energy network for the future, *Environmental Report: Marine Cable Route*.

Swaffield, D.J., Lewin, P.L. & Sutton, S.J., 2008. Methods for rating directly buried high voltage cable circuits, *IET Gener. Transm. Distrib.,* 2**,** 393-401.

Turcotte, D.L. & Schubert, G., 2002. Geodynamics, *Cambridge University Press, Cambridge UK*.

UK House of Commons: Energy and Climate Change Committee, 2011. A European Supergrid, *The stationery office limited, London,* 1.

Van Brakel, J., 1975. Pore space models for transport phenomena in porous media review and evaluation with special emphasis on capillary liquid transport, *Powder Technology,* 11**,** 205-236.

van Landeghem, K.J.J., Baas, J.H., Mitchell, N.C., Wilcockson, D. & Wheeler, A.J., 2014. Reversed sediment wave migration in the irish sea, nw europe: A reappraisal of the validaty of geometry-based predictive modelling and assumptions, *Mar Geol,* 295-298**,** 95-112.

Wentworth, C.K., 1922. A scale of grade and class terms for clastic sediments., *Journal of Geology,* 30**,** 377-392.

Wheatcroft, R.A., Johnson, R.V. & Stevens, A.W., 2007. In situ time-series measurements of sub-seafloor sediment properties, *IEEE J. Oceanic Eng.,* 32**,** 862-871.

Woodside, W. & Messmer, J.H., 1961. Thermal conductivity of porous media: I. unconsolidated sands, II. Consolidated rocks, *J. Appl. Phys.,* 32**,** 1688-1706.

Worzyk, T., 2009. Submarine Power Cables: Design, Installation, Repair, Environmental Aspects, *Springer, Verlag Berlin*

Zimmerman, R.W., 1989. Thermal Conductivity of Fluid-Saturated Rocks, *J Petrol Sci Eng,* 3**,** 219-227.